Accepted Manuscript

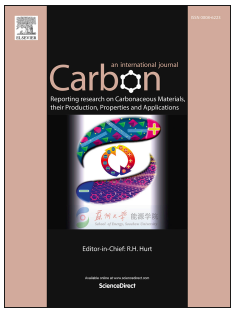

On-off-on fluorescent nanosensor for Fe^{3+} detection and cancer/normal cell differentiation via silicon-doped carbon quantum dots

Ge Gao, Yao-Wen Jiang, Hao-Ran Jia, Jingjing Yang, Fu-Gen Wu

PII: S0008-6223(18)30187-8

DOI: 10.1016/j.carbon.2018.02.063

Reference: CARBON 12899

To appear in: *Carbon*

Received Date: 26 December 2017

Revised Date: 11 February 2018

Accepted Date: 14 February 2018

Please cite this article as: G. Gao, Y.-W. Jiang, H.-R. Jia, J. Yang, F.-G. Wu, On-off-on fluorescent nanosensor for Fe^{3+} detection and cancer/normal cell differentiation via silicon-doped carbon quantum dots, *Carbon* (2018), doi: 10.1016/j.carbon.2018.02.063.

On-off-on fluorescent nanosensor for Fe^{3+} detection and cancer/normal cell differentiation *via* silicon-doped carbon quantum dots

Ge Gao [a, 1], Yao-Wen Jiang [a, 1], Hao-Ran Jia [a], Jingjing Yang [a], Fu-Gen Wu [a, b, *]

[a] *State Key Laboratory of Bioelectronics, School of Biological Science and Medical Engineering, Southeast University, Nanjing 210096, P. R. China*

[b] *Key Laboratory of Developmental Genes and Human Disease of the Ministry of Education of China, Institute of Life Sciences, Southeast University, Nanjing 210096, P. R. China*

* Corresponding author. State Key Laboratory of Bioelectronics, School of Biological Science and Medical Engineering, Southeast University, Nanjing 210096, P. R. China

E-mail addresses: wufg@seu.edu.cn (F. G. Wu).

[1] G. Gao and Y. W. Jiang contributed equally to the work.

ABSTRACT

In this study, an on-off-on fluorescent nanosensor based on carbon quantum dots (or carbon dots, CDs) was successfully fabricated for Fe^{3+} detection and selective imaging of cancerous cells *in vitro* and *in vivo*. The multifunctional CDs were prepared by a one-pot solvothermal treatment of glycerol and a silane molecule (*N*-[3-(trimethoxysilyl)propyl]ethylenediamine, DAMO). The as-prepared CDs exhibited excellent fluorescence (FL) properties and favorable biocompatibility, and could realize wash-free cell imaging both *in vitro* (e.g., for bacterial and fungal cells) and *in vivo* (e.g., for zebrafish embryos). On the other hand, the CDs showed a rapid fluorescence response and good selectivity towards Fe^{3+}, with a linear detection in the concentration range of 0.1–100 μM and a low detection limit of 16 nM. Besides, detection of Fe^{3+} in living cells and zebrafish was also successfully realized by the CDs. Moreover, the mixed solution of CDs and Fe^{3+} (CDs/Fe^{3+}) could efficiently distinguish cancerous cells from normal ones based on the reductive environment of cancerous cell, mainly the difference in the content of glutathione (GSH). More importantly, GSH also realized the enhanced fluorescence signals of CDs/Fe^{3+} in tumor site *in vivo* after intravenous injection, indicating the potential of CDs/Fe^{3+} for imaging-guided precision cancer therapy.

1. Introduction

Fe^{3+}, an essential trace element in plants and animals, plays crucial roles in many biochemical processes, such as regulation of cellular metabolism, oxygen transport in hemoglobin, electron transfer, and enzyme catalysis [1−3]. Besides, the metabolic reprogramming under Fe^{3+} deficiency is related to the functional alteration of essential cell compartments, including mitochondria and chloroplasts. More importantly, abnormal Fe^{3+} levels are relevant to cancer and other diseases such as anemia, arthritis, intelligence decline, diabetes, kidney damage, and heart failure [4−8]. Thus simple, sensitive, and accurate detection of Fe^{3+} in living cells is vital for the early identification and diagnosis of these diseases. Conventional strategies for Fe^{3+} detection, such as atomic absorption spectrometry (AAS) [9], inductively coupled plasma mass spectrometry (ICP-MS) [10], and voltammetry [11], involve complex instrumentation and preparation procedures, which limit their applications. Recently, several fluorescent probes have been developed to detect Fe^{3+}, such as organic dyes [12,13], semiconductor quantum dots [14], metal nanoclusters/nanoparticles [15,16], and fluorescent metal organic frame-based probes [17]. However, the preparations of these probes often require specialized synthetic skills and/or complicated purification procedures. Besides, most of them cannot realize Fe^{3+} detection in living cells and *in vivo*. Therefore, it is necessary to design novel probes possessing excellent photostability, biocompatibility, and high sensitivity for Fe^{3+} detection in living cells and *in vivo*.

Meanwhile, photoluminescent nanomaterials, such as fluorescent nanoclusters [18−20] and semiconductor quantum dots (QDs) [21−23], have become research hotspots due to their unique optical characteristics. However, they are limited by the photobleaching and/or toxicity issues for further application [24−26]. As a type of recently developed nanomaterials, carbon quantum dots (or carbon dots, CDs) have gained ever-increasing attention in bioimaging [27,28], antibacterial [29,30], drug delivery [31−35], microbial live/dead differentiation [36,37], photo- and electrocatalytic water splitting [38,39], and metal ion/glucose detection [40−44] as a result of their unique and tunable photoluminescence (PL), excellent photostability,

appreciable biocompatibility, facile synthesis, and easy surface functionalization [45,46]. In recent years, fluorescent sensors based on CDs for Fe^{3+} detection are attracting more interest because of their rapid response, high sensitivity, and convenient monitoring [47−50]. However, there have been few reports of using CDs for Fe^{3+} detection in living cells and *in vivo*. Thus, the development of CDs used for Fe^{3+} detection in living cells and *in vivo* would draw much attention and is a highly challenging goal.

On the other hand, early detection of cancer can extend patient survival through the therapeutic treatment in the early stages of the disease [51−53]. In addition, intraoperative imaging of tumors, in which surgeons employ fluorophores to identify tumor-positive margins and lymph nodes containing metastases, plays an important role in precision cancer therapy. For better specificity to cancerous cells, QDs, upconversion nanoparticles (UCNPs), or gold nanoparticles (AuNPs) are usually conjugated with the targeting moieties such as peptides, aptamers, and/or small molecules, which enable the nanoparticulate probes to bind specifically to the targets of interest [54−56]. However, these cancerous/normal cell differentiation approaches are usually only suitable for some specific cell types, which limits their further applications. Besides, it has been reported that various tumors express enhanced levels of the radical scavenger glutathione (GSH) as compared with normal tissues [57]. Thus developing detection methods based on the difference in the GSH concentration between cancerous and normal cells is applicable to various types of cells and urgently needed.

Herein, we report a facile solvothermal process to prepare silicon and nitrogen co-doped multifunctional carbon dots (CDs) that use glycerol as the carbon source and solvent medium, and an organosilane molecule *N*-[3-(trimethoxysilyl)propyl]ethylenediamine (DAMO) as the passivation agent. The obtained CDs with amine groups on the surface possess excellent aqueous dispersibility and stability, good photostability, favorable biocompatibility, and easily modifiable surface. Besides, the one-step solvothermal synthesis is simple, convenient, cost-effective, and eco-friendly. Furthermore, the CDs can be used for labeling

different types of microorganism (bacteria and fungi) and zebrafish embryos, indicating their universal cell imaging capability. Moreover, the obtained CDs show a selective and sensitive fluorescence response to Fe^{3+} and have been used for sensitive detection of Fe^{3+} in living cells and zebrafish. More importantly, the mixed solution of CDs and Fe^{3+} (CDs/Fe^{3+}) could efficiently distinguish cancerous cells from normal ones based on the reductive environment of cancerous cell, mainly the difference in their cellular glutathione (GSH) *in vitro* and *in vivo* (Fig. 1), providing a method for efficient cancer diagnosis.

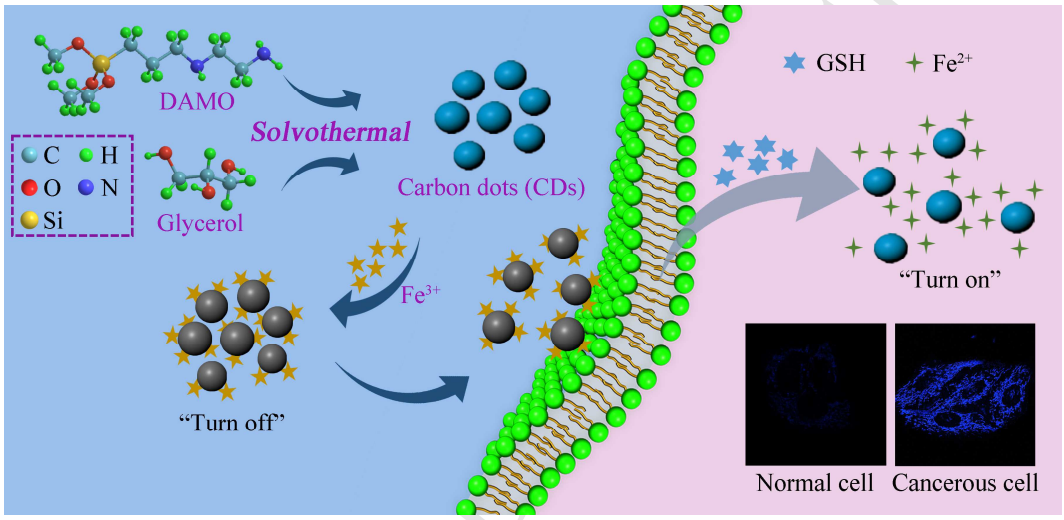

Fig. 1. Schematic illustration of the synthesis of CDs and their applications for Fe^{3+} detection and cancer/normal cell differentiation based on the "on-off-on" fluorescence response property of the CDs.

2. Experimental section

2.1. Materials

Glycerol, dimethyl sulfoxide (DMSO), $AgNO_3$, $Cr(NO_3)_3$, $CuCl_2$, $Pb(NO_3)_2$, $CaCl_2$, $MgCl_2$, $MnSO_4$, $FeCl_2$, $ZnSO_4$, $FeCl_3$, $CdCl_2$, $Hg(NO_3)_2$, glycine, and human serum albumin (HSA) were purchased from Aladdin Chemistry Co. Ltd. (China). Quinine sulfate, buthionine sulfoximine (BSO, a GSH synthesis inhibitor), *N*-methylmaleimide (NMM, a GSH scavenger), and *α*-lipoic acid (LPA, a GSH synthesis enhancer) were obtained from Sigma Aldrich (St. Louis, MO, USA). *N*-[3-(Trimethoxysilyl)propyl]ethylenediamine (DAMO),

(3-(4,5-dimethyl-2-thiazolyl)-2,5-diphenyl-2-*H*-tetrazolium bromide) (MTT), and fluorescein isothiocyanate (FITC) were obtained from J&K Chemical Ltd. (China). All aqueous solutions were prepared using Millipore deionized (DI) water. Human liver cancer cells (Hep G2) and human lung cancer cells (A549) were obtained from Cell Resource Center of Shanghai Institute for Biological Sciences (Chinese Academy of Sciences, Shanghai, China). Human normal liver cells (L02) and mouse cervical cancer cells (U14) were purchased from the American Type Culture Collection (ATCC, Manassas, VA). Human normal lung cells (AT II) was obtained from Medical School of Southeast University. *Staphylococcus aureus* (*S. aureus*), *Escherichia coli* (*E. coli*), *Trichoderma reesei* (*T. reesei*), and *Saccharomyces cerevisiae* (*S. cerevisiae*) cells were from China Center of Industrial Culture Collection (CICC, Beijing, China). Zebrafish embryos were obtained from Eze-Rinka Co. Ltd. (Nanjing, China).

2.2. Synthesis of CDs

The CDs were synthesized according to our reported method [58]. Briefly, 1.5 mL of DAMO was added to 10 mL of glycerol, followed by a degassing process with nitrogen for 2 min. After a 260 ^{o}C, 12 h thermal process, the cooled solid residue was added with 20 mL DI water. The CD solution was collected by centrifugation at 8000 rpm for 10 min and then purified with a dialysis membrane (molecular weight cut-off: ~1 kDa) for 2 days. Finally, CDs were freeze-dried and stored at room temperature for use.

2.3. Characterization of CDs

Transmission electron microscopy (TEM) images were obtained via a Tecnai G2 20 transmission electron microscope. A zetasizer instrument (Nano ZS, Malvern Instruments, United Kingdom) was used for recording the hydrodynamic diameters and zeta potentials. Fourier transform infrared (FTIR) spectroscopic analysis was performed on an FTIR spectrometer (Nicolet iS50, Thermo Scientific, USA). X-ray photoelectron spectroscopy (XPS) analysis was operated at a PHI Quantera II X-ray

photoelectron spectrometer (Ulvac-Phi). The ultraviolet−visible (UV−vis) absorption spectra were collected using a UV-2600 spectrophotometer (Shimadzu). Fluorescence spectra were obtained using a Shimadzu RF-5301PC spectrofluorophotometer.

2.4. Measurement of quantum yield (QY)

The QY of the CDs was measured using quinine sulfate (QY: 54%) as a reference, which was dissolved in a 0.1 M H_2SO_4 aqueous solution. The relative QY of CDs was calculated using the follow equation (Eq. 1):

$$\varphi_c = \varphi_s \times \frac{A_s}{I_s} \times \frac{I_c}{A_c} \times \frac{\eta_c^{\,2}}{\eta_s^{\,2}} \qquad (1)$$

where φ represents QY, A is the optical density, I is the integrated emission intensity and η is the solvent refractive index. The subscripts "c" refers to the CDs and "s" refers to quinine sulfate solutions.

2.5. Cytotoxicity assay

AT II cells were cultured in complete Dulbecco's modified Eagle's medium (cDMEM, containing 10% fetal bovine serum) at 37 ^{o}C under 5% CO_2. To evaluate the cytotoxicity of CDs, Hep G2 cells were seeded in 96-well plate with a cell density of 5×10^3 cells per well. After overnight incubation, the culture media were removed, and CDs in fresh culture media were added at different concentrations (0, 5, 10, 20, 50, 100, and 200 μg/mL). After incubation for another 24 h, a standard MTT assay was used to examine the cell viability. The cytotoxicity tests of CDs toward L02, A549, and Hep G2 cells were similar as described above.

To study the toxicity of CDs towards microorganisms, log phase cells of *S. aureus* (optical density at 600 nm, OD_{600} = 0.5) were inoculated with 1 : 10 into 100 μL of fresh lysogeny broth (LB) medium containing different concentrations of CDs (10, 20, 50, 100, 200, 300, and 500 μg/mL) and seeded into a 96-well plate. Then the bacteria were incubated for 24 h at 37 ^{o}C in a shaking incubator. The metabolic activity of bacteria was evaluated by OD_{600}, which was recorded through a microplate reader (Thermo-Scientific, Multiskan FC, USA) every 2 h. To test the cytotoxicity of CDs

toward *E. coli* and *S. cerevisiae*, similar experiments were carried out as mentioned above.

2.6. Cell growth measurement using a real-time cellular analysis (RTCA) system

The iCELLigence system (ACEA Biosciences Inc.) was used to monitor the influences of CDs on the growth of AT II cells in real time. Cell index was used to quantify cell status based on detected cell-electrode impedance. For real-time cell proliferation monitoring, 200 μL of cDMEM was added to each well of a E-plate L8 (8 wells) to obtain background reading, and then AT II cells were seeded in E-plate L8 with a density of 1.5×10^4 cells per well. When the cell index value reached ~1, 10 μL CD solution was introduced to each well to reach different final concentrations (0, 20, 50, 100, or 200 μg/mL).

2.7. Hemolysis assay

The mouse red blood cells (RBCs) were obtained by removing serum from the blood by centrifugation and washing as reported previously [59]. Then RBCs suspended with phosphate-buffered saline (PBS) were mixed with equivalent CD solution at a final CDs concentration of 5, 10, 20, 50, 100, or 200 μg/mL. RBCs in PBS solution and in 1% Triton X-100 solution were set as the negative control and the positive control, respectively. After the mixtures were incubated at 37 °C for 2 h and centrifugated for 5 min, the absorbance at 450 nm of these supernatants was measured using a microplate reader. The hemolysis percentage was calculated using the following formula:

$$\text{Hemolysis\%} = (I_{\text{sample}} - I_{\text{negative control}})/(I_{\text{positive control}} - I_{\text{negative control}}) \times 100\%$$

where I represents the absorbance at 450 nm.

2.8. Microorganism imaging

S. aureus and *E. coli* were used as the representative Gram-positive and Gram-negative bacteria, respectively. The two types of bacteria were cultured in fresh LB medium (5 mg/mL yeast extract, 10 mg/mL tryptone, and 10 mg/mL NaCl). *T.*

reesei and *S. cerevisiae* as two representative fungi were cultured in potato dextrose broth (PDB) medium (200 mg/mL potatoes, 20 mg/mL dextrose, and 20 mg/mL agar powder) and Yeast Extract Peptone Dextrose (YPD) medium (20 mg/mL peptone, 10 mg/mL yeast extract, and 20 mg/mL glucose), respectively. The bacterial and fungal cells were collected and mixed with CDs in culture medium (final concentration: 50 μg/mL). Then, the bacterial cells were incubated at 37 ^{o}C in a shaking incubator, while the fungal cells were cultured at 28 ^{o}C. After incubation for 30 min, the bacterial and fungal cells were collected by centrifugation at 6000 rpm for 5 min, and washed with PBS for 3 times before being imaged using confocal laser scanning microscopy (CLSM) via a confocal microscope (TCS SP8, Leica, Germany).

2.9. Detection of Fe^{3+} using CDs

The detection of Fe^{3+} was conducted in aqueous solutions at room temperature. Weighted $FeCl_3$ solid was dissolved in DI water (adding 1–2 drops 1 M HCl) to prepare the Fe^{3+} stock solution with a final concentration of 10 mM. Different concentrations of $FeCl_3$ solution (0, 0.2, 2, 4, 10, 40, 100, 200, 400, 1000, and 2000 μM) were obtained by diluting the stock solution with DI water. The CDs were diluted with DI water to reach a concentration of 100 μg/mL for the fluorescence measurements. The CD solution was mixed with one of the above $FeCl_3$ solutions in equal volume (the final concentration of CDs: 50 μg/mL). The fluorescence emission spectra of the above mixed solutions were collected under 350 nm excitation. To confirm the selectivity of CDs toward Fe^{3+}, other metal ion solutions were examined in a similar way. The Fe^{3+} detection selectivity and sensitivity of CDs in the coexistence of other metal ions were also tested. The selective analysis was performed for CDs in the presence of Fe^{3+} ions (1 mM) and one of the following ions (1 mM): Pb^{2+}, Mn^{2+}, Ag^{+}, Fe^{2+}, Mg^{2+}, Cd^{2+}, Cr^{3+}, Hg^{2+}, Ca^{2+}, Cu^{2+}, and Zn^{2+}, and in the presence of the mixture of Fe^{3+} ions and all the above-mentioned ions. The sensitivity analysis was tested in the mixed solution containing all the above-mentioned ions. Besides, to mimic the physiological environment in the cell, the mixed solution containing abundant cellular cations (1 mM Na^{+}, 1 mM K^{+}, 1 mM Mg^{2+}, and 1 mM

Ca^{2+}) and trace metal cations (50 μM Mn^{2+}, 50 μM Fe^{2+}, and 50 μM Zn^{2+}) [40] was also used to test the Fe^{3+} detection sensitivity and selectivity of CDs.

2.10. Fe^{3+} detection in living cells

MCF-7 cells in cDMEM were seeded in a 96-well plate at a density of 5×10^3 cells per well. The cells were cultured for 24 h in an incubator with 5% CO_2 at 37 ^oC. Then the CD solution in cDMEM (50 μg/mL) was used to replace the culture medium in each well. After incubation for 10 min, the cells were rinsed with PBS for 3 times and incubated with a 0.9% NaCl solution containing 5, 20, or 100 μM Fe^{3+} for another 30 min. The cells were then imaged by a confocal microscope using a 63× objective.

2.11. Fe^{3+} detection in zebrafish

Zebrafish at 5 dpf (days post fertilization) were cultured at 28.5 ^oC using standard zebrafish E3 culture medium (5 mM NaCl, 0.33 mM $CaCl_2$, 0.33 mM $MgSO_4 \cdot 7H_2O$, and 0.17 mM KCl) in a 96-well plate. Then the culture medium in each well was replaced with the standard zebrafish E3 culture medium containing the CD solution in the culture medium (200 μg/mL). After incubation for 4 h, the larvae were rinsed with PBS for 3 times and incubated with 5, 20, or 100 μM Fe^{3+} in the culture medium for another 2 h. Then the fluorescence of each larva was observed under a confocal microscope using a 10× objective.

2.12. Cell imaging using CDs/Fe^{3+} solution

Before cell imaging, the fluorescence response of CDs/Fe^{3+} to GSH was first studied. Different concentrations of GSH (0, 20, 40, 100, 200, and 400 μM) were first prepared and then the CDs/Fe^{3+} solution was mixed with one of the above GSH solutions in equal volume (the final concentration: CDs: 50 μg/mL, Fe^{3+}: 20 μM). The fluorescence emission spectra of the above mixed solutions were collected under 350 nm excitation. The fluorescence response of CDs/Fe^{3+} to glycine or human serum albumin (HSA) was evaluated in a similar way.

The cancerous cells (A549 and Hep G2) and normal cells (AT II and L02) were

cultured separately in cDMEM. The cells were seeded in a 96-well plate at a density of 5×10^3 cells per well. After incubation for 24 h, the culture medium in each well was replaced with CDs/Fe^{3+} (CDs: 50 μg/mL, Fe^{3+}: 20 μM) in culture medium for 10 min. Then CLSM and flow cytometry were used to analyze the cellular fluorescence in different cells. For comparison purposes, these cells without treatment were also analyzed by flow cytometry. To further explore the influence of GSH on cellular fluorescence, the A549 cancerous cells were pretreated with BSO (100 μM) for 1 h or NMM (500 μM) for 20 min followed by incubation with CDs/Fe^{3+} (CDs: 50 μg/mL, Fe^{3+}: 20 μM) for 10 min, while the AT II normal cells were pretreated with LPA (500 μM) for 24 h and further treated with/without NMM (500 μM) for 20 min followed by incubation with CDs/Fe^{3+} (CDs: 50 μg/mL, Fe^{3+}: 20 μM) for 10 min. Then CLSM was used to analyze the cellular fluorescence after different treatments. For the co-culture assay, cancerous cells (A549 or Hep G2 cells) and normal cells (AT II or L02 cells) with a cell number ratio of 1 : 1 were co-cultured in 96-well plate for 24 h and the following incubaion and imaging steps were similar with those mentioned above.

2.13. In vivo and ex vivo fluorescence imaging

For animal experiments, female nude mice were purchased from Yangzhou University Medical Centre (Yangzhou, China) and used under the approval of the Animal Care Committee of Southeast University. The animal experiments were conducted in compliance with the Regulations for the Administration of Affairs Concerning Experimental Animals of China. To establish the subcutaneous tumor model, U14 carcinoma cells (2×10^7, suspended in 100 μL of PBS) were inoculated onto the back of the nude mice. For intratumoral administration, 100 μL of PBS or CDs/Fe^{3+} solution (CDs: 50 μg/mL, Fe^{3+}: 20 μM) was adopted. For intravenous administration, 100 μL of PBS or CDs/Fe^{3+} solution (CDs: 10 mg/kg, Fe^{3+}: 4 mM/kg) was adopted. Then the treated mice were imaged by a Cri Maestroin *in vivo* imaging system with an excitation wavelength of 480 nm and an emission wavelength of 580 nm. For *ex vivo* imaging, representative mice from different groups

were sacrificed at the specific time point, and then tumor and major organs including heart, liver, spleen, lung and kidneys were taken out to conduct *ex vivo* fluorescence imaging. To see whether the CDs themselves can target tumor, *ex vivo* fluorescence images of major organs and tumors excised from the mice after treatment with CDs were also provided. *Ex vivo* imaging was performed on the same instrument with an excitation wavelength of 420 nm and an emission wavelength of 520 nm.

2.14. Statistical analyses

Data were presented as mean values ± standard errors (SD) from 3 independent experiments in every group. One-way ANOVA analysis followed by Tukey's post test was used to determine the difference of cellular fluorescence between cancerous and normal cells (*$P < 0.05$, **$P < 0.01$, or ***$P < 0.001$).

3. Results and discussion

3.1. Characterization of CDs

The CDs were obtained by heating DAMO in glycerol at 260 ^{o}C for 12 h (Fig. 1), and the as-prepared CDs could be homogeneously dispersed in various solvents. First, the morphology of CDs was characterized by TEM. The TEM image (Fig. 2a) and the corresponding histogram of size distribution (Fig. 2b) illustrate that CDs have an average size of ~6.1 nm with uniform spherical shape. The hydrodynamic diameters of CDs in water, 0.9% NaCl solution, and PBS measured via the dynamic light scattering (DLS) were 14.2 ± 0.9 nm, 14.9 ± 1.3 nm, and 15.1 ± 1.8 nm, respectively (Fig. S1), indicating the stability of CDs in different media. In addition, the hydrodynamic diameters of CDs in the three media remained nearly unchanged during 90-day period, further confirming the excellent aqueous stability of the CDs (Fig. S2). Furthermore, FTIR spectroscopy was used to investigate the surface functional groups of CDs. As shown in Fig. 2c, the CDs possess absorption bands of O–H/N–H stretching vibration (3650–3000 cm^{-1}), C–H stretching vibration (3000–2800 cm^{-1}), N–H bending vibration (1610 cm^{-1}), and Si–O/C–O stretching vibration (1112 cm^{-1}, also observed in the spectrum of DAMO), indicating the

existence of amino groups and various other moieties (such as O–H, C–H, Si–O, and C–O) in the CDs. Moreover, XPS analysis was carried out to further identify the components of CDs. The high resolution C 1s spectrum of CDs can be well-fitted into C–Si (283.5 eV), C–C (284.7 eV), C–N (285.3 eV), and C=O (287.1 eV) (Fig. 2d). The N 1s XPS spectrum of CDs can be decomposed into peaks at 398.2 eV (C–N–C), 399.1 eV (N–C), and 400.3 eV (N–H) (Fig. 2e). Two main peaks in the Si 2p spectrum indicate the binding energy at 100.5 eV for Si–C bond and 102.4 eV for Si–O bond (Fig. 2f). These results further confirm that N and Si atoms are present in CDs, in good agreement with the FTIR results. Besides, as shown in Fig. 2g, the zeta potential values of CDs in water, 0.9% NaCl solution, and PBS were measured to be +8.9 mV, −3.2 mV, and −7.2 mV, respectively. The differences of these zeta potential values are due to the differences in pH and/or ionic strength of the three different aqueous solutions [60].

The optical properties of the obtained CDs were also characterized. The UV−vis absorption spectrum of CDs shown in Fig. 2h exhibits an intense absorption band at 273 nm, which is attributed to the π–π* transition of aromatic C−C bonds. In addition, the broad absorption band at ~328 nm is ascribed to the n–π* transition of C=O bonds [61]. In the fluorescence spectra, CDs have optimal excitation and emission wavelengths at 350 and 442 nm, respectively (Fig. 2h). Moreover, the excitation-dependent photoluminescence behavior was observed in Fig. 2i, which is due to the surface state and band gap of CDs [62]. Besides, the CDs preserved stable fluorescence in solutions with a wide range of ionic strengths and pH values. Particularly, the fluorescence intensity only changed slightly by ~9% and ~11% with ionic strength varying from 0 to 2.5 M and pH value increasing from 2 to 12, respectively (Fig. S3). Besides, the stability of the fluorescence intensity of CDs in NaCl solution at different pH values and after storage for different time periods were also evaluated. As shown in Fig. S4, the fluorescence intensity only changed by ~14% with pH value increasing from 2 to 12 and ~3% during 30-day period, indicating the stable fluorescence of CDs in various conditions. Furthermore, the photostability of FITC (a commercial dye) and CDs was evaluated. As shown in Fig. S5, the

fluorescence signal of FITC was quickly quenched after 3-min UV irradiation due to severe photobleaching. Comparatively, the CDs still maintained ~50% of the original fluorescence intensity after 10-min UV irradiation, indicating the superior photostability of CDs compared to FITC. The QY of CDs was as high as 45 % (using quinine sulfate as a reference). Both high QY and robust photostability make the CDs suitable for further bioimaging applications.

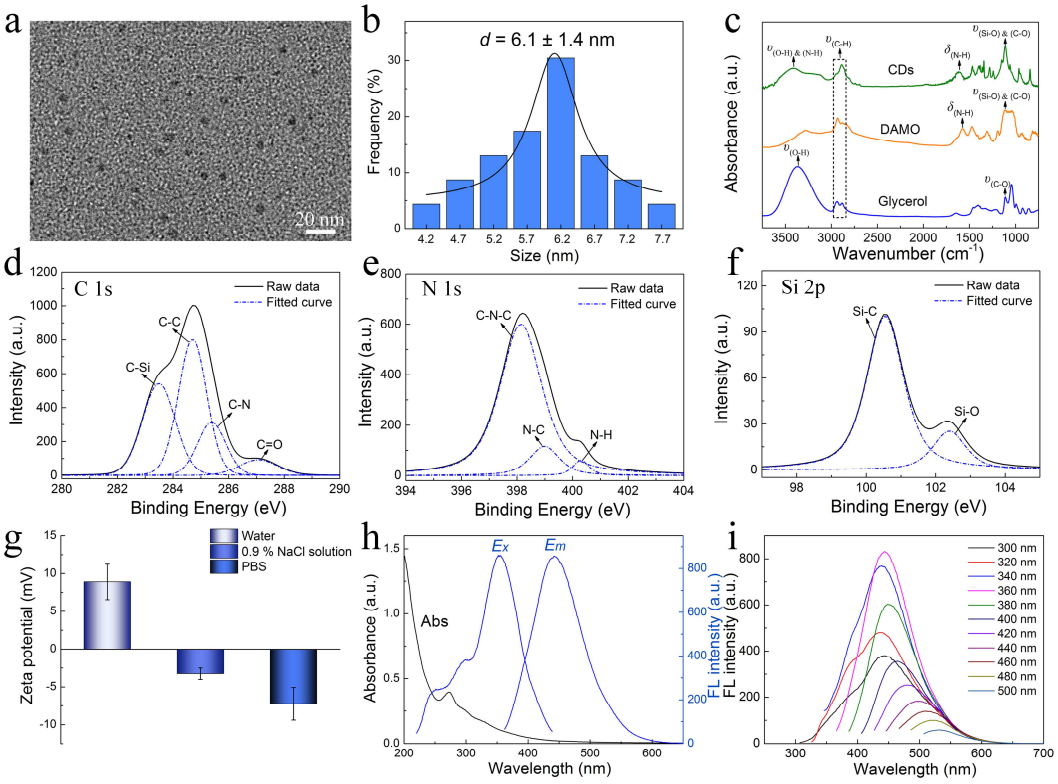

Fig. 2. (a) TEM image and (b) the corresponding size distribution of DAMO CDs. (c) FTIR spectra of CDs, DAMO, and glycerol. (d–f) High resolution XPS spectra of DAMO CDs: (d) C 1s, (e) N 1s, and (f) Si 2p. (g) Zeta potentials of DAMO CDs (50 μg/mL) in water, 0.9% NaCl solution, and PBS, respectively. (h) UV–vis absorption spectrum and fluorescence excitation/emission spectra of DAMO CDs (50 μg/mL). (i) Fluorescence spectra of DAMO CDs under different excitation wavelengths.

3.2. Cytotoxicity of CDs

To evaluate *in vitro* cytocompatibility of DAMO CDs, we investigated the cytotoxicity of DAMO CDs via MTT, RTCA, and hemolysis assays. The MTT results

in Fig. 3a indicate that the CDs showed negligible cytotoxicity at the concentration of 200 μg/mL or below. The RTCA results (Fig. 3b) show that CDs induced little cell death even at the concentration of 200 μg/mL, which is consistent with the MTT assay results. Furthermore, RBCs maintained their normal discoid shape after treatment with CDs at concentrations of up to 200 μg/mL (Fig. 3c) and the hemolysis assay show that the CDs had negligible hemolytic activity toward RBCs even when their concentration was up to 200 μg/mL (Fig. 3d), indicating the good hemocompatibility of the CDs.

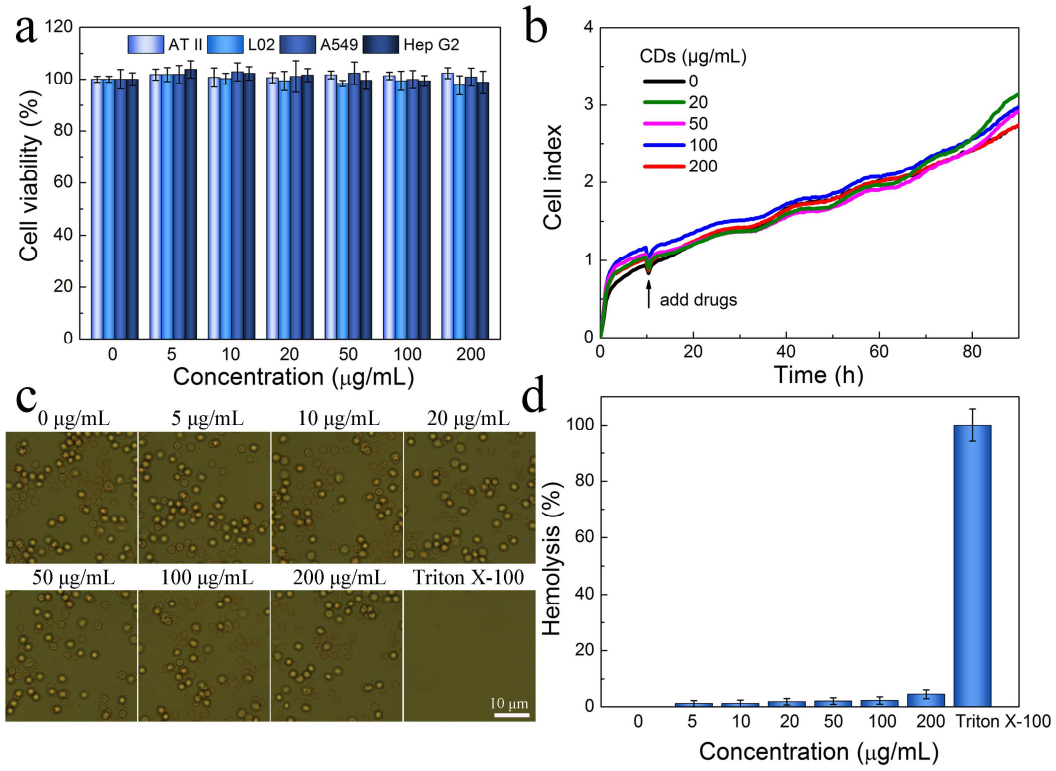

Fig. 3. *In vitro* biocompatibility evaluation. (a) MTT assay results of AT II, L02, A549, and Hep G2 cells after treatment with various concentrations of CDs for 24 h. (b) RTCA results of AT II cells treated with CDs at different dosages. (c) Optical images of RBCs incubated with different concentrations of CDs. (d) Hemolysis percentages of RBCs in the presence of various concentrations of CDs. Triton X-100 was used as the positive control.

3.3. Imaging of microorganisms using CDs

Considering the small size and excellent fluorescence properties (such as strong fluorescence emission and good photostability) of CDs, we further tested their

imaging ability toward microorganisms (including bacterial and fungal cells). Typically, as shown in Fig. S6, after incubation with CDs (50 μg/mL) for 30 min, both bacterial (*E. coli* and *S. aureus*) and fungal cells (*S. cerevisiae* and *T. reesei*) exhibited intense blue, green, or red fluorescence under 405, 488, or 552 nm laser excitation, respectively. Besides, the results in Fig. S7 show that the CDs had negligible cytotoxicity to bacterial (*S. aureus* and *E. coli*) and fungal (*S. cerevisiae*) cells even when the concentration of CDs reached 100 μg/mL.

3.4. Detection of Fe^{3+} using CDs

It has been reported that the specific covalent binding can be formed between Fe^{3+} and amine groups [63]. Given that the as-prepared CDs are rich in amine groups, it is worthy to study whether the fluorescence of CDs can response to Fe^{3+} selectively and sensitively. As illustrated in Fig. 4a and b, except for Fe^{3+}, which decreased the FL intensity of CDs to 16%, no obvious changes in the fluorescence quenching values (F/F_0) of CDs were observed after adding different metal ions (including Hg^{2+}, Cr^{3+}, Cd^{2+}, Mg^{2+}, Fe^{2+}, Ag^{+}, Mn^{2+}, Zn^{2+}, Pb^{2+}, Ca^{2+}, and Cu^{2+}), suggesting that the CDs were suitable for Fe^{3+} detection. In addition, the fluorescence spectra of the CDs after adding different concentrations of Fe^{3+} are shown in Fig. 4c. With the increasing of the Fe^{3+} concentration from 0.1 μM to 1 mM, the fluorescence intensity of CDs (at 450 nm) decreased gradually. A linear relationship was observed for the fluorescence decrease ($(F_0 - F)/F_0$) and the Fe^{3+} concentration (C, ranging from 0.1 to 100 μM) (Fig. 4d), with the linear regression equation of $(F_0 - F)/F_0 = 0.00148C + 0.01604$ (the correlation coefficient, R^2, is 0.997) and a detection limit of 16 nM (calculated at a signal-to-noise ratio of 3 [48,64,65]). Furthermore, as shown in Fig. S8a and b, the CDs exhibited similar responses to Fe^{3+} alone, the mixtures of Fe^{3+} and one of the following ions: Pb^{2+}, Mn^{2+}, Ag^{+}, Fe^{2+}, Mg^{2+}, Cd^{2+}, Cr^{3+}, Hg^{2+}, Ca^{2+}, Cu^{2+}, and Zn^{2+}, and the mixture of Fe^{3+} and all these ions, indicating the high selectivity of CDs in sensing Fe^{3+} with no significant interferences from these coexisting ions. Besides, the CDs also showed a sensitive fluorescence response to Fe^{3+} in the mixed solution of the above-mentioned ions with a detection limit of 18 nM (Fig. S8c and d). To mimic

the physiological environment in the cell, we also tested the sensitivity and selectivity of CDs for metal ions in the mixed solution containing 1 mM Na^+, 1 mM K^+, 1 mM Mg^{2+}, 1 mM Ca^{2+}, 50 μM Mn^{2+}, 50 μM Fe^{2+}, and 50 μM Zn^{2+}. As shown in Fig. S9, the CDs also showed a selective and sensitive fluorescence response to Fe^{3+} in the mixed solution of metal ions with a detection limit of 16 nM. The above results demonstrated that the CDs could detect Fe^{3+} in the coexistence of various metal ions with high selectivity and sensitivity.

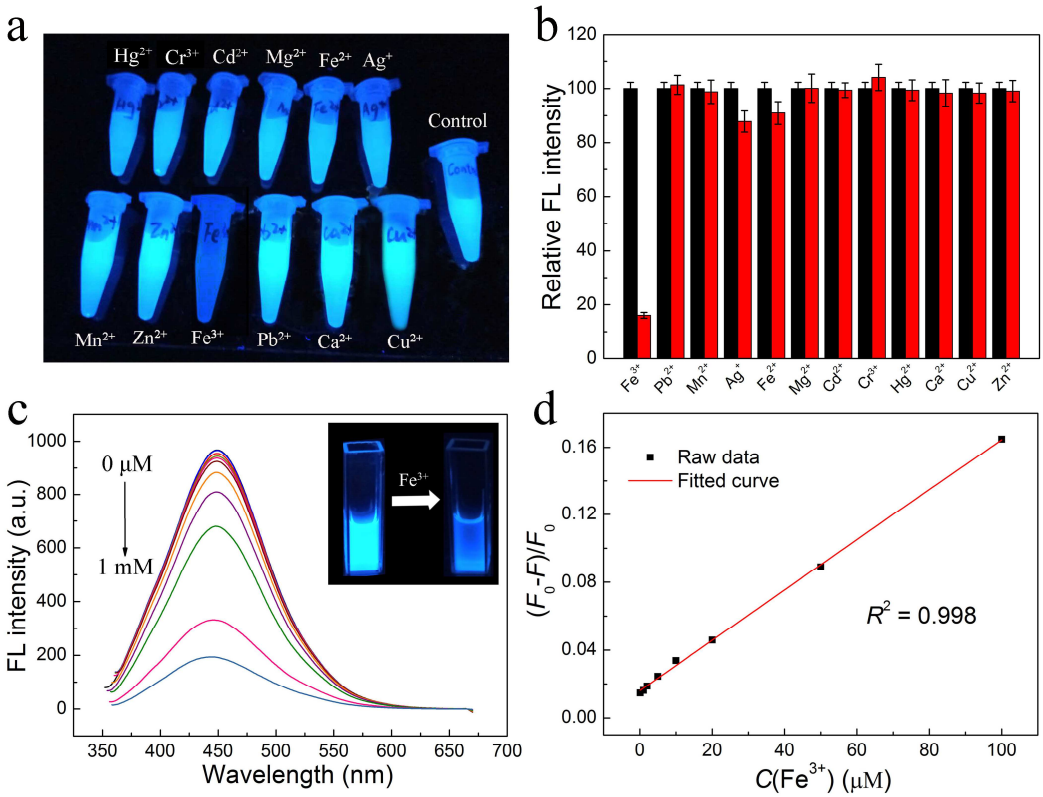

Fig. 4. (a) Photographs of CDs (30 μg/mL) alone (Control) or after incubation with different kinds of metal ions (1 mM) under the irradiation of a UV light (302 nm). (b) Relative fluorescence intensities of the CDs in the absence (black column) and presence (red column) of different metal ions (1 mM). (c) Fluorescence spectra of CDs in the presence of Fe^{3+} ion (from top to bottom: 0, 0.1, 1, 2, 5, 10, 20, 50, 100, 200, 500, and 1000 μM). Inset: Images of the DAMO CDs before (left) and after (right) interaction with Fe^{3+} under UV light. (d) Plot of $(F_0 - F)/F_0$ versus the concentrations of Fe^{3+}, $C(Fe^{3+})$, and the linear calibration.

3.5. Mechanism for Fe^{3+} detection by CDs

Generally, fluorescence can be quenched through dynamic quenching or static quenching. Both dynamic quenching and static quenching through ground-state complex formation model can be theoretically described by the Stern-Volmer equation (Eq. 2):

$$\frac{F}{F_0} = 1 + K_{SV}[Q] \qquad (2)$$

where F_0 and F are the steady-state fluorescence intensity in the absence and presence of the quencher, respectively, K_{SV} is the Stern-Volmer constant and [Q] is the concentration of CDs. In this study, as shown in Fig. S10, there was an excellent linear relationship between the fluorescence intensity ratio (F/F_0) of CDs and the concentration of Fe^{3+}, indicating that the quenching mechanism was dynamic quenching or static quenching. To further investigate the mechanism of fluorescence quenching of CDs in the presence of Fe^{3+}, UV−vis absorption spectra and fluorescence lifetime experiments were performed. Fig. 5a shows that the experimental curve (the absorption spectrum of CDs/Fe^{3+}) did not coincide with the theoretical curve (the physical addition of the spectra of CD solution and Fe^{3+} solution), indicating the formation of stable metal ion–CDs complexes. Besides, as shown in Fig. 5b, after addition of Fe^{3+}, the lifetime of CDs (τ_1: 3.5 ns, τ_2: 10.1 ns) was almost the same as that without Fe^{3+} (τ_1: 3.6 ns, τ_2: 10.6 ns), excluding the existence of dynamic quenching. These results suggest that static quenching occurred between CDs and Fe^{3+}. In detail, Fe^{3+} ion can interact with the amine groups on the surface of the CDs, and then the electrons in the excited state will transfer to the half-filled 3d orbitals of Fe^{3+}, leading to the fluorescence quenching of CDs with the nonradiative electron–hole annihilation [49].

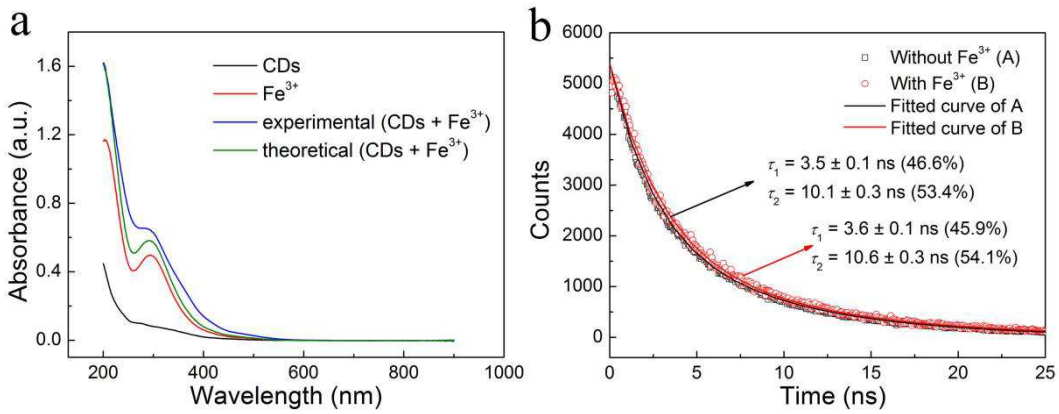

Fig. 5. (a) UV–vis absorption spectra of CDs (5 μg/mL), Fe^{3+} (200 μM), the experimental curve (the absorption spectrum of CDs/Fe^{3+}), and the theoretical curve (the physical addition of the spectrum of CD solution and Fe^{3+} solution). (b) Fluorescence decays of the CDs in the absence or presence of Fe^{3+} (*Ex*: 350 nm, *Em*: 450 nm).

3.6. Intracellular detection of Fe^{3+}

It has been reported that Fe^{3+} overload and deficiency can disturb the cellular homeostasis, resulting in various diseases [7]. Therefore, to establish a sensitive and convenient method for intracellular detection of Fe^{3+} is very important. Here we would like to test if CDs can be used to detect the intracellular Fe^{3+}. After incubation with CDs (50 μg/mL), HeLa cells were treated with 0, 5, 20, or 100 μM Fe^{3+} for 30 min. As revealed by CLSM, the fluorescence intensity of CDs in HeLa cells decreased with the increasing concentration of exogenous Fe^{3+} (Fig. 6a). Besides, the results of the cellular fluorescence intensity obtained by flow cytometry (Fig. 6b and c) agree well with those by CLSM. The above results indicate that the CDs are suitable for Fe^{3+} semiquantitative detection in living cells.

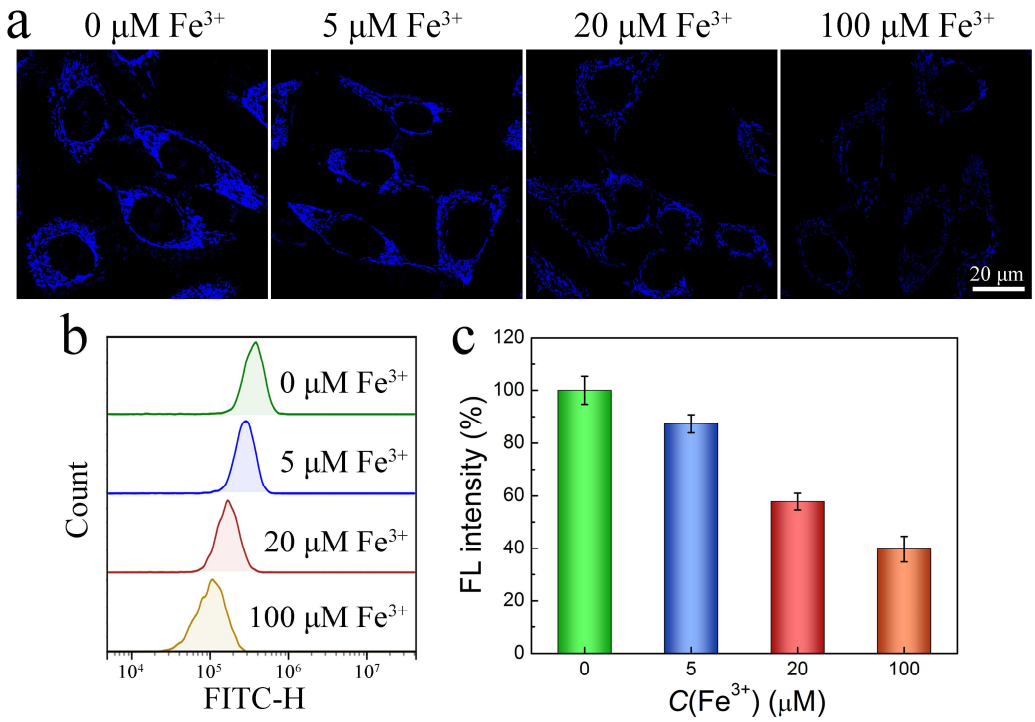

Fig. 6. (a) CLSM images of HeLa cells treated with CDs (50 μg/mL) for 10 min, and then incubated with 0, 5, 20, or 100 μM Fe^{3+} for 30 min. The confocal images were taken after washing the cells with PBS for 3 times. (b) Flow cytometric analysis of the cellular fluorescence after treatment with 0, 5, 20, and 100 μM Fe^{3+} for 30 min, respectively. (c) The corresponding statistics of the flow cytometric results in (b).

3.7. Fe^{3+} detection in zebrafish

Encouraged by the successful detection of intracellular Fe^{3+} using CDs, we would like to further determine whether CDs can be applied for Fe^{3+} detection *in vivo*. Here zebrafish was selected as a model organism for the research. Similar to the *in vitro* experiments, zebrafish were pretreated with CDs (200 μg/mL) for 4 h and then incubated with 0, 5, 20, or 100 μM Fe^{3+} in E3 culture medium for 2 h. As shown in Fig. 7a, the fluorescence intensity of CDs in zebrafish decreased gradually with the increasing concentration of exogenous Fe^{3+}, which was also confirmed by the fluorescence statistics results (Fig. 7b). The above results demonstrate that CDs can realize the *in vivo* semiquantitative detection of Fe^{3+}.

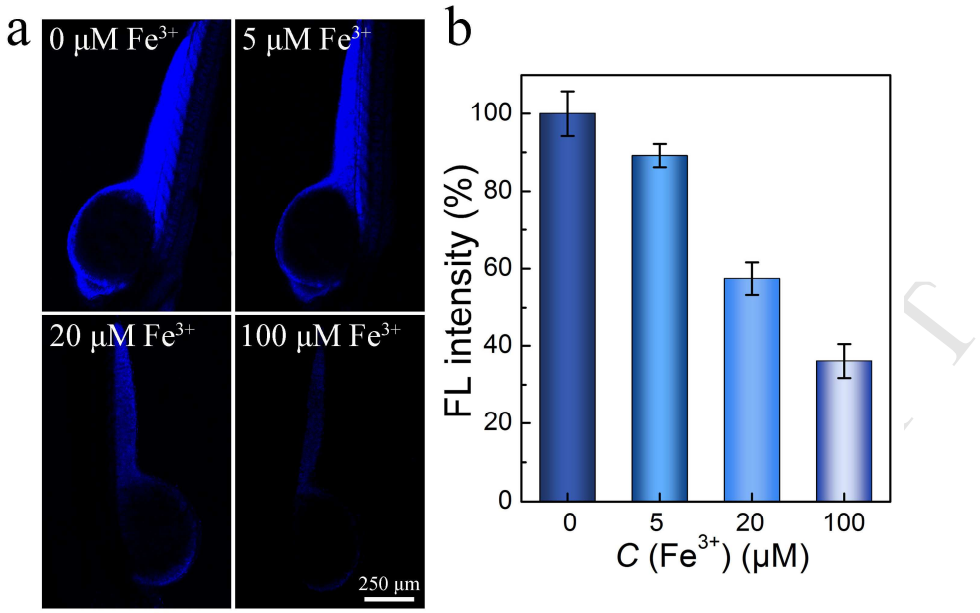

Fig. 7. (a) CLSM images of zebrafish treated with CDs (200 μg/mL) for 4 h, and then incubated with 0, 5, 20, or 100 μM Fe^{3+} for 2 h. (b) The corresponding average fluorescence statistics of the CLSM images in (a).

3.8. Normal/cancerous cell differentiation using CDs/Fe^{3+}

Recent studies have demonstrated the reductive environment of cancerous cells [66−68]. Besides, as compared with normal tissues, various tumors express enhanced levels of GSH [57], which possesses high reduction ability in organisms. Meanwhile, based on the high Fe^{3+} detection selectivity of CDs, we expect that normal/cancerous cell differentiation can be achieved using CDs/Fe^{3+} mixture, which will restore the fluorescence of CDs in cancerous cells due to a higher degree of Fe^{3+} reduction. To verify this hypothesis, we first studied whether the fluorescence of the mixed solution (CDs/Fe^{3+}) could response to GSH. As shown in Fig. S11, with the concentration of GSH increasing from 0 μM to 200 μM, the fluorescence intensity of the mixed solution (CDs/Fe^{3+}) gradually increased, indicating the interaction between Fe^{3+} and GSH. Besides, to explore the effects of substances with amine groups on the fluorescence of CDs/Fe^{3+}, we used two amine-containing biomolecules, glycine, and HSA, to test the response. As shown in Fig. S12, the increase in the fluorescence of CDs/Fe^{3+} caused by glycine or HSA was negligible compared with that caused by GSH. Then normal cells (AT II and L02) and cancerous cells (A549 and Hep G2)

were stained with the CDs/Fe^{3+} mixture (CDs: 50 μg/mL, Fe^{3+}: 20 μM) under the same conditions followed by confocal imaging. The results in Fig. 8a show that strong blue fluorescence was observed in cancerous cells (A549 and Hep G2). In sharp contrast, almost no fluorescence was observed in normal cells (AT II and L02). Besides, to exclude the interference of cellular autofluorescence, the fluorescence intensity of different cells (AT II, A549, L02, and Hep G2) without treatment was first analyzed by flow cytometry (Fig. S13). It can be seen that the autofluorescence intensities of these cells were almost the same. Then the cellular fluorescence intensity of these cells treated with CDs/Fe^{3+} was further analyzed by flow cytometry and the results are shown in Fig. 8b and c. Obviously, the fluorescence intensity of cancerous cells was much stronger than that of normal cells, indicating that CDs/Fe^{3+} is a highly effective fluorescent probe for specific staining of cancerous cells. To further verify the effect of GSH on the normal/cancerous cell differentiation, cells were pretreated with BSO (a GSH synthesis inhibitor), NMM (a GSH scavenger), or LPA (a GSH synthesis enhancer) and then incubated with CDs/Fe^{3+}. As shown in Fig. S14, addition of BSO or NMM resulted in a significant decrease of the fluorescence intensity in A549 cancerous cells. In parallel experiments, a clear fluorescence emission enhancement for AT II normal cells treated with LPA was observed. When NMM was further added to the LPA-treated AT II cells, a distinct decrease of fluorescence intensity was observed. Thus, the above results indicated that GSH played an important role in the cellular fluorescence-based normal/cancerous cell differentiation.

To mimic the physiological environment, normal cells (AT II or L02) and cancerous cells (A549 or Hep G2) were co-cultured in the same well [58,69−71]. After incubation for 24 h, the culture medium in each well was replaced with a fresh medium containing CDs/Fe^{3+} (CDs: 50 μg/mL, Fe^{3+}: 20 μM). Interestingly, only cancerous cells showed bright blue emission while normal cells emitted only feeble fluorescence (Fig. 9), suggesting that CDs/Fe^{3+} can be used to differentiate cancerous cells from normal ones in a tumor environment-mimic situation, which is very important for precision cancer therapy.

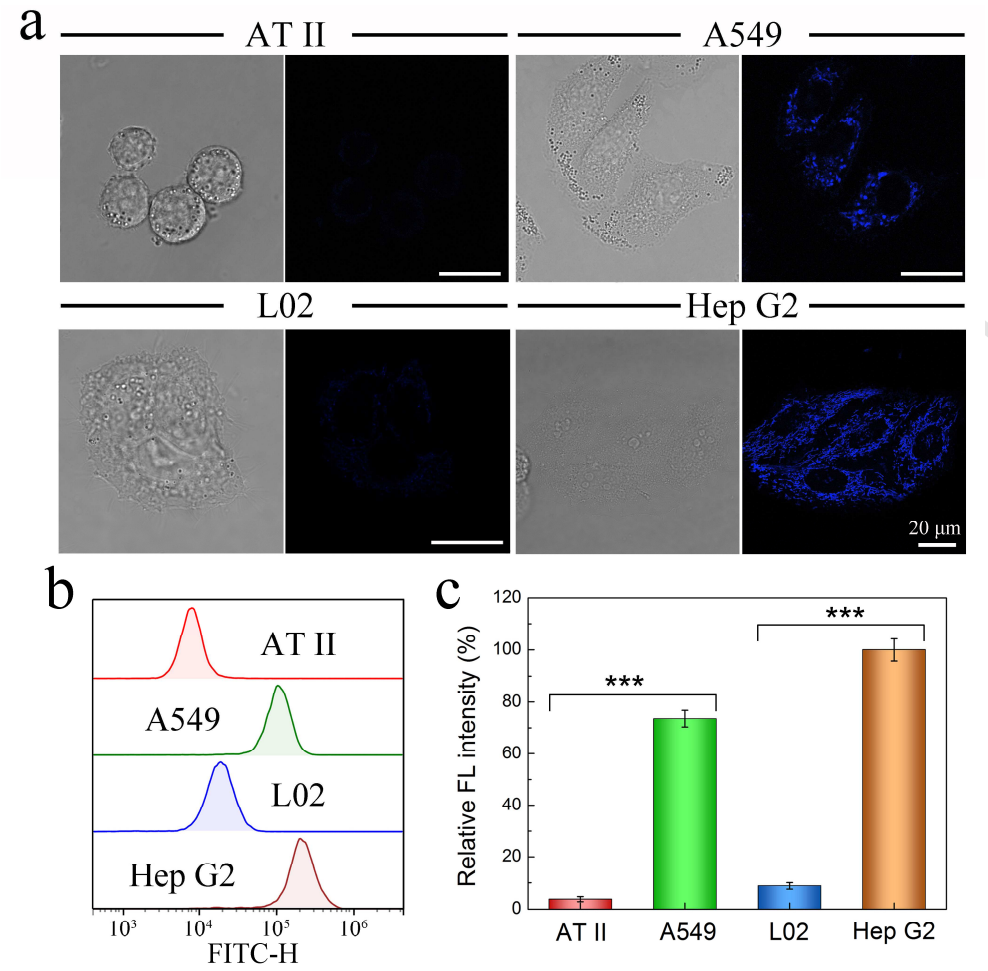

Fig. 8. (a) CLSM images and (b) flow cytometric analysis results of different cells (AT II, A549, L02, and Hep G2) treated with CDs/Fe^{3+} (CDs: 50 μg/mL, Fe^{3+}: 20 μM) for 10 min. (c) The corresponding average fluorescence intensities derived from the flow cytometric data in (b). ***$P < 0.001$, one-way ANOVA.

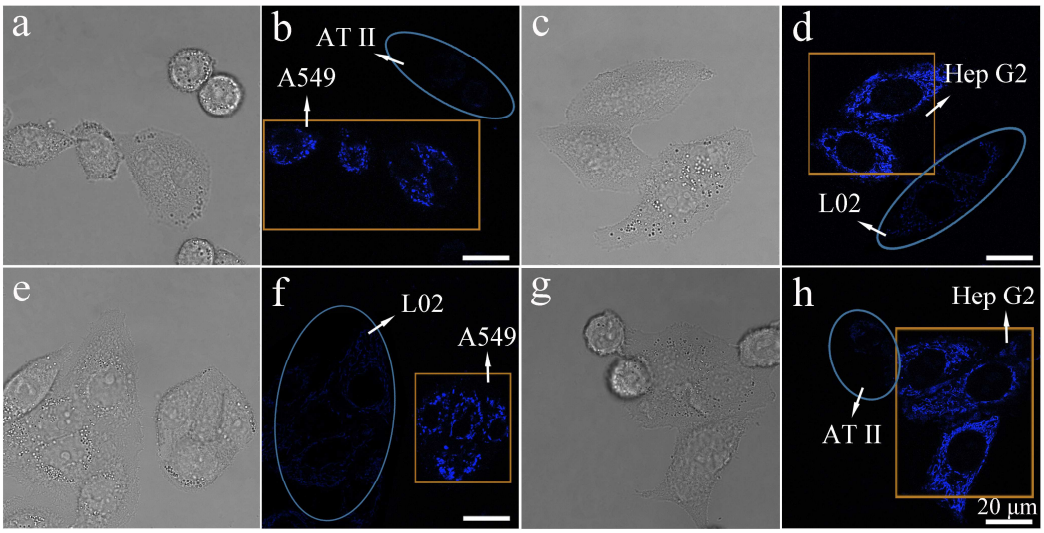

Fig. 9. Bright-field (a, c, e, and g) and the corresponding fluorescence images (b, d, f, and h) of different combinations of cancer cells (A549 or Hep G2) and normal cells (AT II or L02) in cDMEM with CDs/Fe^{3+} (CDs: 50 μg/mL, Fe^{3+}: 20 μM). The yellow rectangles and blue circles are used to mark the positions of cancerous cells and normal cells, respectively.

3.9. In vivo and ex vivo imaging

Motivated by the *in vitro* results, we then evaluated the feasibility of utilizing CDs/Fe^{3+} for tumor-specific imaging *in vivo*. First, the normal tissue and tumor region of a nude mouse bearing subcutaneous U14 xenograft tumor were injected with CDs/Fe^{3+} (dose: CDs: 10 mg/kg, Fe^{3+}: 4 mM/kg), respectively, and then imaged under an animal imaging system at 1 h postinjection. As shown in Fig. 10a, the fluorescence intensity of CDs/Fe^{3+} in the tumor region was much stronger than that in the normal tissue, which was further verified by the result of *ex vivo* tissue imaging (Fig. 10b). Thus, the above results suggest that CDs/Fe^{3+} can realize enhanced fluorescence imaging in the tumor region.

To further testify if CDs/Fe^{3+} can be used as an *in vivo* diagnostic agent through intravenous (i.v.) injection, nude mice bearing U14 tumors were intravenously injected with PBS or CDs/Fe^{3+} (dose: CDs: 10 mg/kg, Fe^{3+}: 4 mM/kg) and then imaged by an animal imaging system at 4 h postinjection. As for the CDs/Fe^{3+}-treated group, only the tumor area exhibited a strong fluorescence signal at 4 h postinjection,

while no detectable signal was observed in the PBS-treated group (Fig. 10c). In addition, nude mice intravenously injected with PBS or CDs/Fe^{3+} were sacrificed at 4 h postinjection. *Ex vivo* imaging in Fig. 10d reveal that the fluorescence intensity in the tumor was much stronger that that in major organs (heart, liver, spleen, lung, or kidneys), which was confirmed by the quantified results (Fig. 10e). In comparison, CDs alone could not achieve tumor accumulation (Fig. S15). The above results clearly demonstrate that CDs/Fe^{3+} achieved tumor accumulation through the enhanced permeability and retention (EPR) effect and exhibited an enhanced fluorescence signal in tumor site under the reductive environment of cancerous cell, mainly the effect of GSH.

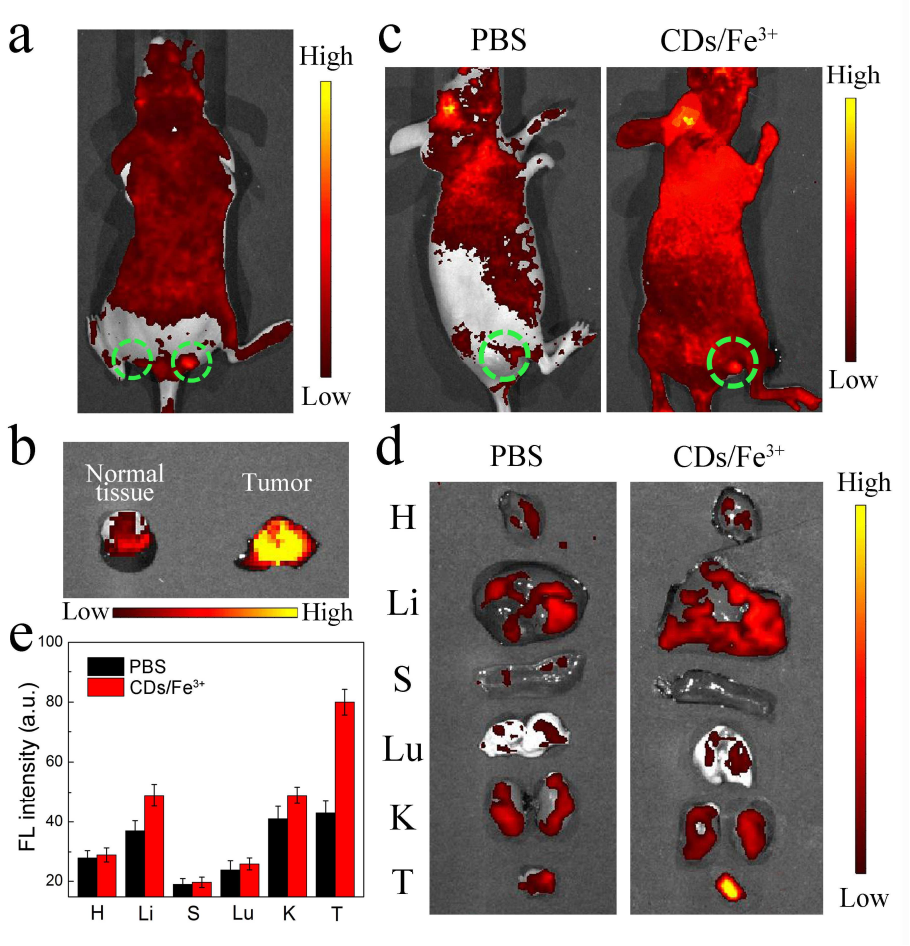

Fig. 10. *In vivo* and *ex vivo* fluorescence imaging. (a) *In vivo* fluorescence image of a nude mouse at 1 h after injection of CDs/Fe^{3+} into normal tissue (the left flank marked by a dotted circle) and tumor (the right flank marked by a dotted circle). (b) *Ex vivo* fluorescence image of normal tissue and tumor excised from the mouse in (a). (c) Real time fluorescence imaging

of nude mice after i.v. injection of PBS or CDs/Fe^{3+} at 4 h postinjection. The tumor regions are marked by dotted circles. (d) *Ex vivo* fluorescence images of major organs and tumors excised from the two mice in (c). H, Li, S, Lu, K, and T represent heart, liver, spleen, lung, kidneys, and tumor, respectively. (e) Average fluorescence intensities in major organs and tumors in (d).

4. Conclusions

To summarize, an on-off-on fluorescent nanosensor based on CDs was successfully designed and synthesized for Fe^{3+} detection and selective imaging of cancerous cells *in vitro* and *in vivo*. In our design, a novel type of CDs was prepared by a one-pot solvothermal treatment of glycerol (the solvent and carbon source) and DAMO (the passivation agent). The CDs, synthesized through a facile, cheap, and environment-friendly thermal process, were remarkably water-dispersible and excellently stable even under extreme pH values, high ionic strengths, and light illumination. The CDs could be used as a novel chemosensor for the highly sensitive detection of Fe^{3+} with a detection limit as low as 16 nM. It is supposed that the Fe^{3+}-mediated FL quenching is attributed to the nonradiative electron−hole annihilation. Besides, the results for monitoring Fe^{3+} in mammalian cells and zebrafish indicate that the CDs can be used as an efficient probe for Fe^{3+} detection in living systems. Moreover, CDs/Fe^{3+} could selectively image the cancerous cells due to the reductive environment of cancerous cell, mainly the higher levels of GSH in cancerous cells. More importantly, CDs/Fe^{3+} achieved tumor accumulation through the EPR effect and displayed an enhanced fluorescence signal in tumor site, indicating its potential for use in imaging-guided precision cancer therapy. The designed nanosensor based on CDs is promising as an efficient platform for clinical diagnosis.

Notes

The authors declare no competing financial interest.

Acknowledgments

This work was supported by grants from the National Natural Science Foundation of China (21673037), Natural Science Foundation of Jiangsu Province (BK20170078), Innovative and Entrepreneurial Talent Recruitment Program of Jiangsu Province, Fundamental Research Funds for the Central Universities, Scientific Research Foundation of Graduate School of Southeast University (YBJJ1778) and Six Talents Peak Project in Jiangsu Province (2015-SWYY-003).

References

[1] M. W. Hentze, M. U. Muckenthaler, B. Galy, C. Camaschella, Two to tango: regulation of mammalian iron metabolism, Cell 142 (1) (2010) 24−38.

[2] S. Fletcher, Discovery of a single molecule transistor in photosystem II, J. Solid State Electrochem. 19 (1) (2015) 241−250.

[3] B. D'Autréaux, N. P. Tucker, R. Dixon, S. Spiro, A non-haem iron centre in the transcription factor NorR senses nitric oxide, Nature 437 (7059) (2005) 769−772.

[4] M. L. Gao, P. H. Xie, L. Y. Wang, X. H. Miao, F. Q. Guo, A new optical sensor for Al^{3+}/Fe^{3+} based on PET and chelation-enhanced fluorescence, Res. Chem. Intermed. 41 (12) (2015) 9673−9685.

[5] G. C. Li, J. Tang, P. G. Ding, Y. Ye, A rhodamine-benzimidazole based chemosensor for Fe^{3+} and its application in living cells, J. Fluoresc. 26 (1) (2016) 155−161.

[6] C. Shen, S. Y. Ge, Y. Y. Pang, F. N. Xi, J. Y. Liu, X. P. Dong, et al., Facile and scalable preparation of highly luminescent N,S co-doped graphene quantum dots and their application for parallel detection of multiple metal ions, J. Mater. Chem. B 5 (32) (2017) 6593−6600.

[7] S. W. Zhang, J. X. Li, M. Y. Zeng, J. Z. Xu, X. K. Wang, W. P. Hu, Polymer nanodots of graphitic carbon nitride as effective fluorescent probes for the detection of Fe^{3+} and Cu^{2+} ions, Nanoscale 6 (8) (2014) 4157−4162.

[8] Y. Q. Zhang, X. D. Li, L. J. Gao, J. H. Qiu, L. P. Heng, B. Z. Tang, et al., Silole-infiltrated photonic crystal films as effective fluorescence sensor for Fe^{3+} and Hg^{2+}, ChemPhysChem 15 (3) (2014) 507−513.

[9] J. E. T. Andersen, A novel method for the filterless preconcentration of iron, Analyst 130 (3) (2005) 385−390.

[10] A. Sussulini, J. S. Becker, J. S. Becker, Laser ablation ICP-MS: application in biomedical research, Mass Spectrom. Rev. 36 (1) (2017) 47−57.

[11] M. M. Abualhaija, C. M. G. van den Berg, Chemical speciation of iron in seawater using catalytic cathodic stripping voltammetry with ligand competition against salicylaldoxime, Mar. Chem. 164 (20) (2014) 60−74.

[12] G. Y. Çiftçi, E. Şenkuytu, M. Bulut, M. Durmuş, Novel coumarin substituted water soluble cyclophosphazenes as "Turn-Off" type fluorescence chemosensors for detection of Fe^{3+} ions in aqueous media, J. Fluoresc. 25 (6) (2015) 1819−1830.

[13] K. Kaur, S. Chaudhary, S. Singh, S. K. Mehta, Azaindole modified imine moiety as fluorescent probe for highly sensitive detection of Fe^{3+} ions, Sens. Actuator B-Chem. 232 (2016) 396−401.

[14] P. Wu, Y. Li, X. P. Yan, CdTe quantum dots (QDs) based kinetic discrimination of Fe^{2+} and Fe^{3+}, and CdTe QDs-fenton hybrid system for sensitive photoluminescent detection of Fe^{2+}, Anal. Chem. 81 (15) (2009) 6252−6257.

[15] J. A. Ho, H. C. Chang, W. T. Su, DOPA-mediated reduction allows the facile synthesis of fluorescent gold nanoclusters for use as sensing probes for ferric ions, Anal. Chem. 84 (7) (2012) 3246−3253.

[16] S. Chaudhary, S. Kumar, A. Umar, J. Singh, M. Rawat, S. K. Mehta, Europium-doped gadolinium oxide nanoparticles: A potential photoluminescencent probe for highly selective and sensitive detection of Fe^{3+} and Cr^{3+} ions, Sens. Actuator B-Chem. 243 (2017) 579−588.

[17] C. X. Yang, H. B. Ren, X. P. Yan, Fluorescent metal-organic framework MIL-53(Al) for highly selective and sensitive detection of Fe^{3+} in aqueous solution, Anal. Chem. 85 (15) (2013) 7441−7446.

[18] J. P. Xie, Y. G. Zheng, J. Y. Ying, Protein-directed synthesis of highly fluorescent gold nanoclusters, J. Am. Chem. Soc. 131 (3) (2009) 888−889.

[19] H. X. Xu, K. S. Suslick, Sonochemical synthesis of highly fluorescent Ag nanoclusters, ACS Nano 4 (6) (2010) 3209−3214.

[20] X. Kang, S. X. Wang, Y. B. Song, S. Jin, G. D. Sun, H. Z. Yu, et al., Bimetallic Au_2Cu_6 nanoclusters: strong luminescence induced by the aggregation of Copper (I) complexes with gold (0) species, Angew. Chem. Int. Ed. 55 (11) (2016) 3611−3614.

[21] Y. L. Li, L. H. Jing, R. R. Qiao, M. Y. Gao, Aqueous synthesis of CdTe nanocrystals: progresses and perspectives, Chem. Commun. 47 (33) (2011) 9293−9311.

[22] R. Freeman, I. Willner, Optical molecular sensing with semiconductor quantum dots (QDs), Chem. Soc. Rev. 41 (10) (2012) 4067−4085.

[23] L. H. Jing, K. Ding, S. V. Kershaw, I. M. Kempson, A. L. Rogach, M. Y. Gao, Magnetically engineered semiconductor quantum dots as multimodal imaging probes, Adv. Mater. 26 (37) (2014) 6367−6386.

[24] B. Hemmateenejad, A. Shahrivar-Kevishahi, F. Shakerizadeh-Shirazi, Reversible photobleaching of gold nanoclusters: a mechanistic investigation, J. Phys. Chem. C 120 (49) (2016) 28215−28223.

[25] V. Venkatesh, A. Shukla, S. Sivakumar, S. Verma, Purine-stabilized green fluorescent gold nanoclusters for cell nuclei imaging applications, ACS Appl. Mater. Interfaces 6 (3) (2014) 2185−2191.

[26] Y. C. Wang, R. Hu, G. M. Lin, I. Roy, K. T. Yong, Functionalized quantum dots for biosensing and bioimaging and concerns on toxicity, ACS Appl. Mater. Interfaces 5 (8) (2013) 2786−2799.

[27] K. Hola, Y. Zhang, Y. Wang, E. P. Giannelis, R. Zboril, A. L. Rogach, Carbon dots−Emerging light emitters for bioimaging, cancer therapy and optoelectronics, Nano Today 9 (5) (2014) 590−603.

[28] Y. Liu, N. Xiao, N. Q. Gong, H. Wang, X. Shi, W. Gu, et al., One-step microwave-assisted polyol synthesis of green luminescent carbon dots as optical nanoprobes, Carbon 68 (2014) 258−264.

[29] J. J. Yang, X. D. Zhang, Y. H. Ma, G. Gao, X. K. Chen, H. R. Jia, et al., Carbon dot-based platform for simultaneous bacterial distinguishment and antibacterial applications, ACS Appl. Mater. Interfaces 8 (47) (2016) 32170−32181.

[30] J. J. Liu, S. Y. Lu, Q. L. Tang, K. Zhang, W. X. Yu, H. C. Sun, et al., One-step hydrothermal synthesis of photoluminescent carbon nanodots with selective antibacterial activity against *Porphyromonas gingivalis*, Nanoscale 9 (21) (2017) 7135−7142.

[31] T. Feng, X. Z. Ai, G. H. An, P. P. Yang, Y. L. Zhao, Charge-convertible carbon dots for imaging-guided drug delivery with enhanced *in vivo* cancer therapeutic efficiency, ACS Nano

10 (4) (2016) 4410−4420.

[32] J. J. Yang, G. Gao, X. D. Zhang, Y. H. Ma, H. R. Jia, Y. W. Jiang, et al., Ultrasmall and photostable nanotheranostic agents based on carbon quantum dots passivated with polyamine-containing organosilane molecules, Nanoscale 9 (40) (2017) 15441−15452.

[33] Y. Shu, J. Lu, Q. X. Mao, R. S. Song, X. Y. Wang, X. W. Chen, et al., Ionic liquid mediated organophilic carbon dots for drug delivery and bioimaging, Carbon 114 (2017) 324−333.

[34] A. D. Zhao, Z. W. Chen, C. Q. Zhao, N. Gao, J. S. Ren, X. G. Qu, Recent advances in bioapplications of C-dots, Carbon 85 (2015) 309−327.

[35] L. Q. Wang, X. Y. Wang, A. Bhirde, J. B. Cao, Y. Zeng, X. L. Huang, et al., Carbon-dot-based two-photon visible nanocarriers for safe and highly efficient delivery of siRNA and DNA, Adv. Healthcare Mater. 3 (8) (2014) 1203−1209.

[36] X. W. Hua, Y. W. Bao, H. Y. Wang, Z. Chen, F. G. Wu, Bacteria-derived fluorescent carbon dots for microbial live/dead differentiation, Nanoscale 9 (6) (2017) 2150−2161.

[37] Y. X. Song, H. Li, F. Lu, H. B. Wang, M. L. Zhang, J. J. Yang, et al., Fluorescent carbon dots with highly negative charges as a sensitive probe for real-time monitoring of bacterial viability, J. Mater. Chem. B 5 (30) (2017) 6008−6015.

[38] X. Q. Wu, C. Zhu, L. P. Wang, S. J. Guo, Y. L. Zhang, H. Li, et al., Control strategy on two-/four-electron pathway of water splitting by multidoped carbon based catalysts, ACS Catal. 7 (3) (2017) 1637−1645.

[39] X. Q. Wu, J. Zhao, S. J. Guo, L. P. Wang, W. L. Shi, H. Huang, et al., Carbon dot and $BiVO_4$ quantum dot composites for overall water splitting *via* a two-electron pathway, Nanoscale 8 (39) (2016) 17314−17321.

[40] A. W. Zhu, Q. Qu, X. L. Shao, B. Kong, Y. Tian, Carbon-dot-based dual-emission nanohybrid produces a ratiometric fluorescent sensor for *in vivo* imaging of cellular copper ions, Angew. Chem. Int. Ed. 51 (29) (2012) 7185−7189.

[41] R. Z. Zhang, W. Chen, Nitrogen-doped carbon quantum dots: facile synthesis and application as a “turn-off” fluorescent probe for detection of Hg^{2+} ions, Biosens. Bioelectron. 55 (2014) 83−90.

[42] S. Chaudhary, S. Kumar, B. Kaur, S. K. Mehta, Potential prospects for carbon dots as a

fluorescence sensing probe for metal ions, RSC Adv. 6 (93) (2016) 90526−90536.

[43] L. Zhou, Y. H. Lin, Z. Z. Huang, J. S. Ren, X. G. Qu, Carbon nanodots as fluorescence probes for rapid, sensitive, and label-free detection of Hg^{2+} and biothiols in complex matrices, Chem. Commun. 48 (8) (2012) 1147−1149.

[44] X. H. Wang, K. G. Qu, B. L. Xu, J. S. Ren, X. G. Qu, Multicolor luminescent carbon nanoparticles: synthesis, supramolecular assembly with porphyrin, intrinsic peroxidase-like catalytic activity and applications, Nano Res. 4 (9) (2011) 908−920.

[45] J. L. Wang, J. J. Qiu, A review of carbon dots in biological applications, J. Mater. Sci. 51 (10) (2016) 4728−4738.

[46] S. Sahu, B. Behera, T. K. Maiti, S. Mohapatra, Simple one-step synthesis of highly luminescent carbon dots from orange juice: application as excellent bio-imaging agents, Chem. Commun. 48 (70) (2012) 8835−8837.

[47] H. J. Zhang, Y. L. Chen, M. J. Liang, L. F. Xu, S. D. Qi, H. L. Chen, et al., Solid-phase synthesis of highly fluorescent nitrogen-doped carbon dots for sensitive and selective probing ferric ions in living cells, Anal. Chem. 86 (19) (2014) 9846−9852.

[48] B. F. Shi, Y. B. Su, L. L. Zhang, M. J. Huang, R. J. Liu, S. L. Zhao, Nitrogen and phosphorus co-doped carbon nanodots as a novel fluorescent probe for highly sensitive detection of Fe^{3+} in human serum and living cells, ACS Appl. Mater. Interfaces 8 (17) (2016) 10717−10725.

[49] Y. Song, C. Z. Zhu, J. H. Song, H. Li, D. Du, Y. H. Lin, Drug-derived bright and color-tunable N-doped carbon dots for cell imaging and sensitive detection of Fe^{3+} in living cells, ACS Appl. Mater. Interfaces 9 (8) (2017) 7399−7405.

[50] J. Yu, C. X. Xu, Z. S. Tian, Y. Lin, Z. L. Shi, Facilely synthesized N-doped carbon quantum dots with high fluorescent yield for sensing Fe^{3+}, New J. Chem 40 (3) (2016) 2083−2088.

[51] L. Wang, Y. Wang, J. I. Wong, T. Palacios, J. Kong, H. Y. Yang, Functionalized MoS_2 nanosheet-based field-effect biosensor for label-free sensitive detection of cancer marker proteins in solution, Small 10 (6) (2014) 1101−1105.

[52] P. M. Kosaka, V. Pini, J. J. Ruz, R. A. da Silva, M. U. González, D. Ramos, et al., Detection of cancer biomarkers in serum using a hybrid mechanical and optoplasmonic

nanosensor, Nat. Nanotechnol. 9 (12) (2014) 1047−1053.

[53] Q. F. Xiao, X. P. Zheng, W. B. Bu, W. Q. Ge, S. J. Zhang, F. Chen, et al., A core/satellite multifunctional nanotheranostic for *in vivo* imaging and tumor eradication by radiation/photothermal synergistic therapy, J. Am. Chem. Soc. 135 (35) (2013) 13041−13048.

[54] R. Savla, O. Taratula, O. Garbuzenko, T. Minko, Tumor targeted quantum dot-mucin 1 aptamer-doxorubicin conjugate for imaging and treatment of cancer, J. Control. Release 153 (1) (2011) 16−22.

[55] T. Zako, H. Nagata, N. Terada, A. Utsumi, M. Sakono, M. Yohda, et al., Cyclic RGD peptide-labeled upconversion nanophosphors for tumor cell-targeted imaging, Biochem. Biophys. Res. Commun. 381 (1) (2009) 54−58.

[56] I. H. El-Sayed, X. H. Huang, M. A. El-Sayed, Surface plasmon resonance scattering and absorption of anti-EGFR antibody conjugated gold nanoparticles in cancer diagnostics: applications in oral cancer, Nano Lett. 5 (5) (2005) 829−834.

[57] T. Schnelldorfer, S. Gansauge, F. Gansauge, S. Schlosser, H. G. Beger, A. K. Nussler, Glutathione depletion causes cell growth inhibition and enhanced apoptosis in pancreatic cancer cells, Cancer 89 (7) (2000) 1440−1447.

[58] G. Gao, Y. W. Jiang, J. J. Yang, F. G. Wu, Mitochondria-targetable carbon quantum dots for differentiating cancerous cells from normal cells, Nanoscale 9 (46) (2017) 18368−18378.

[59] Y. W. Jiang, G. Gao, X. D. Zhang, H. R. Jia, F. G. Wu, Antimicrobial carbon nanospheres, Nanoscale 9 (41) (2017) 15786−15795.

[60] H. Y. Wang, X. W. Hua, H. R. Jia, C. C. Li, F. M. Lin, Z. Chen, et al., Universal cell surface imaging for mammalian, fungal, and bacterial cells, ACS Biomater. Sci. Eng. 2 (6) (2016) 987−997.

[61] S. J. Zhu, Y. B. Song, X. H. Zhao, J. R. Shao, J. H. Zhang, B. Yang, The photoluminescence mechanism in carbon dots (graphene quantum dots, carbon nanodots, and polymer dots): Current state and future perspective, Nano Res. 8 (2) (2015) 355−381.

[62] S. J. Zhu, Q. N. Meng, L. Wang, J. H. Zhang, Y. B. Song, H. Jin, et al., Highly photoluminescent carbon dots for multicolor patterning, sensors, and bioimaging, Angew. Chem. Int. Ed. 52 (14) (2013) 3953−3957.

[63] E. F. Wesp, W. R. Brode, The absorption spectra of ferric compounds. I. the ferric

chloride−phenol reaction, J. Am. Chem. Soc. 56 (5) (1934) 1037−1042.

[64] X. D. Zhang, F. G. Wu, P. D. Liu, N. Gu, Z. Chen, Enhanced fluorescence of gold nanoclusters composed of $HAuCl_4$ and histidine by glutathione: glutathione detection and selective cancer cell imaging, Small 10 (24) (2014) 5170−5177.

[65] X. D. Zhang, X. K. Chen, S. Q. Kai, H. Y. Wang, J. J. Yang, F. G. Wu, et al., Highly sensitive and selective detection of dopamine using one-pot synthesized highly photoluminescent silicon nanoparticles, Anal. Chem. 87 (6) (2015) 3360−3365.

[66] Y. C. Wang, F. Wang, T. M. Sun, J. Wang, Redox-responsive nanoparticles from the single disulfide bond-bridged block copolymer as drug carriers for overcoming multidrug resistance in cancer cells, Bioconjugate Chem. 22 (10) (2011) 1939−1945.

[67] B. Ahn, J. Park, K. Singha, H. Park, W. J. Kim, Mesoporous silica nanoparticle-based cisplatin prodrug delivery and anticancer effect under reductive cellular environment, J. Mater. Chem. B 1 (22) (2013) 2829−2836.

[68] Y. N. Zhong, W. J. Yang, H. L. Sun, R. Cheng, F. H. Meng, C. Deng, et al., Ligand-directed reduction-sensitive shell-sheddable biodegradable micelles actively deliver doxorubicin into the nuclei of target cancer cells, Biomacromolecules 14 (10) (2013) 3723−3730.

[69] Y. Miki, K. Ono, S. Hata, T. Suzuki, H. Kumamoto, H. Sasano, The advantages of co-culture over mono cell culture in simulating *in vivo* environment, J. Steroid Biochem. Mol. Biol. 131 (3) (2012) 68−75.

[70] H. Li, J. Chang, Bioactive silicate materials stimulate angiogenesis in fibroblast and endothelial cell co-culture system through paracrine effect, Acta Biomater. 9 (6) (2013) 6981−6991.

[71] G. Y. Pan, H. R. Jia, Y. X. Zhu, R. H. Wang, F. G. Wu, Z. Chen, Dual channel activatable cyanine dye for mitochondrial imaging and mitochondria-targeted cancer theranostics, ACS Biomater. Sci. Eng. 3 (12) (2017) 3596−3606.